

Orbitally resolved superconductivity in real space: FeSe

Fang Yang,^{1,2,*} Jasmin Jandke,² Peter Adelman,³ Markus J. Klug,⁴ Thomas Wolf,³ Sergey Faleev,⁵ Jörg Schmalian,^{4,3} Matthieu Le Tacon,³ Arthur Ernst,^{5,6} and Wulf Wulfhekel²

¹*Institute for Nanoelectronic Devices and Quantum Computing,
Fudan University, Songhu Rd. 2005, 200438 Shanghai, P.R. China*

²*Physikalisches Institut, Karlsruhe Institute of Technology,
Wolfgang-Gaede Str. 1, 76131 Karlsruhe, Germany*

³*Institut für Festkörperphysik, Karlsruhe Institute of Technology, 76344 Karlsruhe, Germany*

⁴*Institut für Theorie der Kondensierten Materie, Karlsruhe Institute of Technology,
Wolfgang-Gaede Str. 1, 76131 Karlsruhe, Germany*

⁵*Max-Planck-Institut für Mikrostrukturphysik,
Weinberg 2, D-06120 Halle, Germany*

⁶*Institute for Theoretical Physics, Johannes Kepler University Linz,
Altenberger Straße 69, 4040 Linz, Austria*

(Dated: May 28, 2019)

Abstract

Multi-orbital superconductors combine unconventional pairing with complex band structures, where different orbitals in the bands contribute to a multitude of superconducting gaps. We here demonstrate a fresh approach using low-temperature scanning tunneling microscopy (LT-STM) to resolve the contributions of different orbitals to superconductivity. This approach is based on STM's capability to resolve the local density of states (LDOS) with a combined high energy and sub unit-cell resolution. This technique directly determines the orbitals on defect free crystals without the need for scatters on the surface and sophisticated quasi-particle interference (QPI) measurements. Taking bulk FeSe as an example, we directly resolve the superconducting gaps within the units cell using a 30 mK STM. In combination with density functional theory calculations, we are able to identify the orbital character of each gap.

In this Letter, we show that by reducing the distance of the tip to the surface, orbitally resolved information on the gap can be obtained by lateral variations of the tunneling spectra within the unit cell. This technique may be very helpful to gain additional information on many multi-band superconductors and the direct observation of the orbitals may clarify some controversies regarding the nature of the involved bands. As a model system to demonstrate this approach, we chose bulk FeSe as it has the simplest crystalline structure among iron-based superconductors and does not require doping to become superconducting [1–5]. The unit cell of FeSe contains a layer of two Fe atoms and two layers Se atoms, one above and one below the Fe plane and the multi-band electronic structure near the Fermi level consists of three hole pockets at the Γ -point and two electron pockets at the M-point [6–11]. It is established that the d_{xz} , d_{yz} , d_{xy} orbitals of Fe dominate the Fermi surface. However, nematic order adds complexity to this material with a structural phase-transition at $T_s = 90$ K from a high-temperature tetragonal phase ($a = b \neq c$, space group: $P4/nmm$) to a low-temperature orthorhombic phase ($a \neq b \neq c$, space group: $Cmma$) with no magnetic ordering. Due to the 0.3% orthorhombic distortion, the unit cell is only of C_2 rotational symmetry with two inequivalent mirror planes (see Figure 1b). As a consequence, the degeneracy between the d_{xz} and d_{yz} orbitals is lifted. A splitting of 50 meV was observed with angle-resolved photoemission spectroscopy (ARPES) [6, 12–17]. The size of the splitting is larger than expected for an orthorhombic lattice distortion [6, 17–19] and was thus attributed to electronic nematicity [16, 17, 20].

Ultimately, a complex nature of superconductivity in FeSe arises, that occurs below a critical temperature of ≈ 8 K [21]. The superconducting gap symmetry of single-crystalline FeSe has been discussed widely in the literature. Some report a nodal gap [22, 23] and more recent papers a nodeless pairing symmetry [24–27]. Even though there are some variations with respect to the size of the various gaps, a uniform observation is the multigap structure. Using QPI patterns, Sprau et al. could identify two anisotropically gapped bands without nodes of mainly d_{yz} character [25]. However, no consensus about the exact orbital contributions of each gap has been reached [27–29]. To address these questions, we focus on STM images and spectra spatially resolved within the unit cell.

Figure 1a shows an STM topography of the sample cleaved in situ at low temperatures. The white dots reflect the upper (or lower) Se atoms of the surface layer, depending on the tunneling conditions [30]. The regular pattern illustrates the translational symmetry of the

lattice of FeSe with practically no defects. To first order, the tunneling current in STM is given by the LDOS of the sample leaking out into the vacuum integrated over the bias energy window, as has been shown by Tersoff and Hamann [31]. Thus, STM topography in constant current mode reflects the iso-surface of the energy integrated LDOS. For low sample bias, the LDOS of a normal conductor does not vary significantly and can be considered a constant. Thus, STM topography at low bias directly represents the iso-surface of the electron density at the Fermi level E_F decaying into the vacuum. In the superconducting state, only the quasi-particle states outside the gap Δ contribute to the LDOS. If the bias voltage U is set significantly above Δ , the integrated LDOS in the superconducting state is nearly that of the normal state. In that respect, the STM image reflects the LDOS near E_F of the normal state. In theory, the LDOS of the normal state is given by the single particle excitations of the electrons, i.e. by the single-particle spectral function weighted by the form factor of Bloch states, at the respective energy. These states take into account the translational symmetry of the crystal as they are a product of a lattice periodic wave function $u_\lambda^{\mathbf{k}}(\mathbf{r})$ and a plane wave $e^{i\mathbf{k}\mathbf{r}}$, where \mathbf{k} is the wave vector, \mathbf{r} is the position in real space and λ denotes the quantum numbers related to the atomic states as the orbital degrees of freedom or the spin. The band structure describes the energy E as function of \mathbf{k} and λ . In order to study multi-band superconductors, either ARPES is used to directly measure $E(\mathbf{k})$. Alternatively, laterally resolved STM spectra of the sample including scatterers on the surface causing quasi-particle interference patterns can be imaged. By Fourier transforming the observed QPI patterns into momentum space, information on the bands can be obtained. Since QPI shows the scattering intensity of the impurities as function of momentum transfer \mathbf{q} between the initial and final wave vectors [25], one typically compares QPI patterns calculated from theoretical band structures with the experimental one to reveal the nature of the underlying bands. Thus, QPI mainly focusses on the band dispersion.

We here take the opposite approach to gain complementary information. In samples without defects, the Bloch states cause a LDOS that does not vary from unit cell to unit cell (no QPI patterns). Instead, the atomic part of the wave function causes LDOS variations within the unit cell directly reflecting the quantum numbers λ . Thus, the atomically resolved image of Fig. 1a basically shows the iso-surface of $\sum_\lambda |u_\lambda^{\mathbf{k}}(\mathbf{r})|^2$. Figure 1c shows a topographic map of the size of 2×2 unit cells. The unit cell and its symmetry are indicated by solid back lines (translational symmetry) and dashed lines (mirror planes). The white

dots represent the positions of the upper Se atoms. The image was created by averaging over 16 individual unit cells using the translational symmetry and by using the two mirror planes. This procedure significantly reduces the statistical noise in the STM data. Besides the Se atoms, a low intensity and finer structure becomes visible. Figure 1d displays an iso-LDOS map within the surface unit cell calculated from first-principles. It was obtained by determining the surface of constant LDOS in the vacuum in front of the surface corresponding to the setpoint conditions of the STM experiment (see Methods). The experimental and calculated maps agree reasonably well (see below for more details).

Figure 2a illustrates the energy dependence of the LDOS near Δ recorded at 30 mK [32]. When taking relatively mild tunneling conditions for tip stabilization ($U=5$ mV and $I=320$ pA, green curve), the dI/dV curves, which are proportional to the LDOS, clearly shows a nodeless gap between $\pm \approx 150 \mu\text{V}$, and two clear coherence peaks at ≈ 2.2 and 1.3 meV in agreement with previous results on the anisotropic gap of FeSe [25, 33]. Thus, we can validate the full gap with our energy resolution of $\approx 24 \mu\text{eV}$. The two shoulders inside the lowest energy coherence peaks stem from the anisotropic gap. Under these mild tunneling conditions, we probe the evanescent Bloch states relatively far from the topmost atoms. It is well established, that far out the LDOS is dominated by s-electrons [34, 35] as s-electrons decay the slowest into the vacuum. Note that due to the lifting of the continuous rotation symmetry by the crystal, the angular momentum is not a strict quantum number and all orbitals partially mix into s-states. When, however, increasing the tunneling conductance by approaching the tip further ($U=5$ mV and $I=1$ nA, blue curve), the contributions of orbitals with larger orbital momentum to the LDOS will increase [35]. As a consequence, the gap spectrum gains more structure. The shoulders develop into coherence peaks and the wider coherence peaks split into several peaks. As will be shown later, this is due to states of different orbital character and different gaps. Most interestingly, when recording dI/dV spectra at low distance at different lateral positions (see Fig. 2b) the intensities of the features but not their energy vary. Note that an increase of the intensity at positive bias goes hand in hand with an increase at the same negative bias. This hints for orbitally selective superconducting gaps.

In order to disentangle the orbital contributions, we carried out the following experiments and calculations. First, we recorded dI/dV spectra within 12 unit cells with a resolution of 11x11 points in the individual unit cell. Similar to the topography, we use translational,

rotational and mirror symmetries to average the data. Figure 3a shows the averaged and symmetrized extracted LDOS. Note, however, that the individual spectra vary within the unit cell, as will be discussed below, but the peak positions observed in the low current spectra can all be found in the averaged high-current spectrum. Next, we decompose the LDOS near E_F from the DFT calculations into contributions of the different orbitals on the afore-mentioned iso-plane of the total LDOS of Fig. 1d. The patterns within the unit cell are displayed in Figure 3c. The calculations include all s, p and d- orbitals. It can be seen, that the composition of the LDOS varies dramatically within the unit cell for the different orbitals. Note that due to the different quantum numbers of the orbitals, no interference terms for the electrons tunneling into the different orbitals (final states) is expected. Thus, the LDOS can be written as a linear combination of the partial LDOS of the different orbitals (see Supplementary). This gives the opportunity to decompose the experimentally observed LDOS patters into their constituents regarding the orbital quantum numbers. Figure 3d displays pairs of the observed pattern and the simulated pattern as well as the weights of the composition of the different orbitals (bar graphs) at energies as indicated. While the s-state still dominates the current, clearly variations of the weights of the other orbitals are observed. These are responsible for the variation of the patterns. The experimental and simulated patterns agree well within the capabilities of STM and our first-principles calculations. The p-states are in general of higher intensity than the d-states. Moreover, the d-states that extend more into the vacuum (d_{z^2} more than d_{xz} and d_{yz}) have a higher intensity. The in-plane d_{xy} and $d_{x^2-y^2}$ states have undetectable weight. This agrees with the expectation of the spatial distribution of the orbitals. Figure 3b plots the contributions of all detected orbitals as function of energy. The s-spectrum agrees nicely with the low-current spectrum of Fig. 2a. Most interestingly, the individual coherence peaks in the data of Fig. 3b show clear selectivity to specific orbitals. For example, the lowest coherence peak at 0.28 meV is mostly of p_x character, and the highest peak at 1.08 meV is mostly of p_z character and the shoulder at 1.12 meV has a large p_y character. These states stem from the p-orbitals of Se. Similarly, the contribution of the Fe d-states to the different coherence peaks varies largely. The coherence peak at 0.82 meV is composed equally of d_{xz} and d_{yz} . In the nematic phase, this is characteristic for the hole pocket at the Γ -point [6, 10, 11, 19, 27–29, 36]. Thus we can attribute this gap to the hole pocket. The coherence peak at 1.12 meV shows a sizeable contribution of d_{yz} but not of d_{xz} . Thus, the symmetry is broken which is

characteristic for the elliptical electron pockets at the M-point and we can associate the gap to the electron pocket.

We hope that our analysis regarding the p-orbitals of Se and their contributions to the bands will stimulate further calculations on the hybridization of the p- and d-states. This would allow to identify more of the coherence peaks. Finally, when the contribution of specific states peaks at a certain bias voltage, QPI patterns recorded at that voltage may also provide momentum information. As such, we see this approach as a method to extend the use of STM in superconductivity research, especially in combination with QPI.

* Electronic address: francoyang1988@163.com

- [1] Hsu, F.-C. *et al.* Superconductivity in the PbO-type structure -FeSe. *Proceedings of the National Academy of Sciences* **105**, 14262–14264 (2008).
- [2] Hirschfeld, P. J., Korshunov, M. M. & Mazin, I. I. Gap symmetry and structure of Fe-based superconductors. *Reports on Progress in Physics* **74**, 124508 (2011).
- [3] Böhmer, A. E. & Kreisel, A. Nematicity, magnetism and superconductivity in FeSe. *Journal of Physics: Condensed Matter* **30**, 023001 (2017).
- [4] Mizuguchi, Y. & Takano, Y. Review of Fe Chalcogenides as the Simplest Fe-Based Superconductor. *Journal of the Physical Society of Japan* **79**, 102001 (2010).
- [5] Coldea, A. I. & Watson, M. D. The Key Ingredients of the Electronic Structure of FeSe. *Annual Review of Condensed Matter Physics* **9**, 125–146 (2018).
- [6] Watson, M. D. *et al.* Emergence of the nematic electronic state in FeSe. *Phys. Rev. B* **91**, 155106 (2015).
- [7] McQueen, T. M. *et al.* Tetragonal-to-Orthorhombic Structural Phase Transition at 90 K in the Superconductor Fe_{1.01}Se. *Phys. Rev. Lett.* **103**, 057002 (2009).
- [8] Watson, M. D., Haghighirad, A. A., Rhodes, L. C., Hoesch, M. & Kim, T. K. Electronic anisotropies revealed by detwinned angle-resolved photo-emission spectroscopy measurements of FeSe. *New Journal of Physics* **19**, 103021 (2017).
- [9] Massat, P. *et al.* Charge-induced nematicity in FeSe. *Proceedings of the National Academy of Sciences* **113**, 9177–9181 (2016).
- [10] Yamakawa, Y., Onari, S. & Kontani, H. Nematicity and Magnetism in FeSe and Other Families

- of Fe-Based Superconductors. *Phys. Rev. X* **6**, 021032 (2016).
- [11] Ishizuka, J., Yamada, T., Yanagi, Y. & no, Y. Fermi Surface, Pressure-Induced Antiferromagnetic Order, and Superconductivity in FeSe. *Journal of the Physical Society of Japan* **87**, 014705 (2018).
- [12] Zhang, P. *et al.* Observation of two distinct d_{xz}/d_{yz} band splittings in FeSe. *Phys. Rev. B* **91**, 214503 (2015).
- [13] Watson, M. *et al.* Evidence for unidirectional nematic bond ordering in FeSe. *Physical Review B* **94**, 201107 (2016).
- [14] Nakayama, K. *et al.* Reconstruction of Band Structure Induced by Electronic Nematicity in an FeSe Superconductor. *Phys. Rev. Lett.* **113**, 237001 (2014).
- [15] Maletz, J. *et al.* Unusual band renormalization in the simplest iron-based superconductor FeSe_{1-x}. *Phys. Rev. B* **89**, 220506 (2014).
- [16] Shimojima, T. *et al.* Lifting of xz/yz orbital degeneracy at the structural transition in de-twinning FeSe. *Phys. Rev. B* **90**, 121111 (2014).
- [17] Suzuki, Y. *et al.* Momentum-dependent sign inversion of orbital order in superconducting FeSe. *Phys. Rev. B* **92**, 205117 (2015).
- [18] Watson, M. D. *et al.* Suppression of orbital ordering by chemical pressure in FeSe_{1-x}S_x. *Phys. Rev. B* **92**, 121108 (2015).
- [19] Watson, M. D. *et al.* Formation of Hubbard-like bands as a fingerprint of strong electron-electron interactions in FeSe. *Phys. Rev. B* **95**, 081106 (2017).
- [20] Kostin, A. *et al.* Imaging orbital-selective quasiparticles in the Hund's metal state of FeSe. *Nature Materials* **17**, 869–874 (2018).
- [21] Hsu, F.-C. *et al.* Superconductivity in the PbO-type structure -FeSe. *Proceedings of the National Academy of Sciences* **105**, 14262–14264 (2008).
- [22] Song, C.-L. *et al.* Direct Observation of Nodes and Twofold Symmetry in FeSe Superconductor. *Science* **332**, 1410–1413 (2011).
- [23] Kasahara, S. *et al.* Field-induced superconducting phase of FeSe in the BCS-BEC cross-over. *PNAS* **111**, 16309–16313 (2014).
- [24] Jiao, L. *et al.* Direct evidence for multi-gap nodeless superconductivity in FeSe. *arXiv preprint arXiv:1605.01908* (2016).
- [25] Sprau, P. O. *et al.* Discovery of orbital-selective Cooper pairing in FeSe. *Science* **357**, 75–80

- (2017).
- [26] Kreisel, A. *et al.* Orbital selective pairing and gap structures of iron-based superconductors. *Phys. Rev. B* **95**, 174504 (2017).
 - [27] Benfatto, L., Valenzuela, B. & Fanfarillo, L. Nematic pairing from orbital-selective spin fluctuations in FeSe. *npj Quantum Materials* **3**, 56 (2018).
 - [28] Kreisel, A., Mukherjee, S., Hirschfeld, P. J. & Andersen, B. M. Spin excitations in a model of FeSe with orbital ordering. *Phys. Rev. B* **92**, 224515 (2015).
 - [29] Mukherjee, S., Kreisel, A., Hirschfeld, P. J. & Andersen, B. M. Model of Electronic Structure and Superconductivity in Orbitally Ordered FeSe. *Phys. Rev. Lett.* **115**, 026402 (2015).
 - [30] Kreisel, A. *et al.* Towards a quantitative description of tunneling conductance of superconductors: Application to LiFeAs. *Phys. Rev. B* **94**, 224518 (2016).
 - [31] Tersoff, J. & Hamann, D. R. Theory of the scanning tunneling microscope. *Phys. Rev. B* **31**, 805–813 (1985).
 - [32] Balashov, T., Meyer, M. & Wulfhekel, W. A compact ultrahigh vacuum scanning tunneling microscope with dilution refrigeration. *Rev. Sci. Instrum.* **89**, 113707 (2018).
 - [33] Chen, G.-Y., Zhu, X., Yang, H. & Wen, H.-H. Highly anisotropic superconducting gaps and possible evidence of antiferromagnetic order in FeSe single crystals. *Phys. Rev. B* **96**, 064524 (2017).
 - [34] Hofer, W. A., Foster, A. S. & Shluger, A. L. Theories of scanning probe microscopes at the atomic scale. *Reviews of Modern Physics* **75**, 1287–1331 (2003).
 - [35] Takahashi, Y. *et al.* Orbital Selectivity in Scanning Tunneling Microscopy: Distance-Dependent Tunneling Process Observed in Iron Nitride. *Phys. Rev. Lett.* **116**, 056802 (2016).
 - [36] Guterding, D., Jeschke, H. O. & Valentí, R. Basic electronic properties of iron selenide under variation of structural parameters. *Phys. Rev. B* **96**, 125107 (2017).
 - [37] Böhmer, A. E., Taufour, V., Straszheim, W. E., Wolf, T. & Canfield, P. C. Variation of transition temperatures and residual resistivity ratio in vapor-grown FeSe. *Phys. Rev. B* **94**, 024526 (2016).
 - [38] Lüders, M., Ernst, A., Temmerman, W. M., Szotek, Z. & Durham, P. J. Ab initio angle-resolved photoemission in multiple-scattering formulation. *J. Phys. Condens. Matter* **13**, 8587–8606 (2001).
 - [39] Perdew, J. P., Burke, K. & Ernzerhof, M. Generalized Gradient Approximation Made Simple.

Phys. Rev. Lett. **77**, 3865– (1996).

Methods

Single crystals of FeSe were prepared by chemical vapor transport using elemental Fe and Se and a eutectic mix of the chlorine salts, KCl and AlCl₃ in a constant temperature gradient [37]. On the single crystals, steel posts were glued and the samples were transferred into ultra high vacuum (UHV). They were cleaved in UHV at a 77 K and were directly inserted into the LT-STM followed by a rapid cool down to the base temperature. STM tips were electrochemically etched from thin W wires and were atomically cleaned by flashing in UHV. dI/dU spectra were obtained by numerical differentiation from $I(U)$ curves to avoid modulation broadening. dI/dU maps have been recorded with a lock-in amplifier and a modulation voltage of $U_{\text{rms}} = 28\mu\text{V}$. Experimental patterns in the unit cell were fitted with calculated patterns using a least-square method.

First-principles calculations were performed using a self-consistent Green function method within the multiple scattering theory specially designed for semi-infinite systems such as surfaces and interfaces [38]. The method utilizes the density functional theory in the generalized gradient approximation [39]. The crystalline structure of the FeSe bulk and surface was adopted from the literature. The vacuum was modelled by layers with empty spheres. The potentials of 10 FeSe units cells and 6 vacuum unit cells were calculated self-consistently with proper boundary conditions for semi-infinite geometry. The LDOS was calculated up to distances of 6Å above the surface. Iso-LDOS surfaces were constructed from the LDOS representing the experimental tunneling conditions using the Tersoff-Hamann approximation [31].

Supplementary Information is linked to the online version of the paper at www.nature.com/nature.

Acknowledgements The authors acknowledge funding by the Deutsche Forschungsgemeinschaft (DFG) under the grant WU 349/12-1, INST 121384/30-1 FUGG (W.W.), SCHM 1031/7-1 (J.S.) and SFB762/3 A04 (A.E.), as well as funding by the Alexander-von-Humboldt foundation (F.Y.).

Author contribution F.Y., J.J. and W.W. conceived the experiments. F.Y. and J.J. carried out the STM experiments. F.Y. and W.W. carried out data analysis. S.F. and A.E. performed ab-initio calculations. T.W. and P.A. grew the samples. J.S. and M.K. performed analytical calculations. F.Y., J.J. and W.W. wrote the draft. All authors contributed in discussions and finalizing the manuscript.

Author information Reprints and permissions information is available at www.nature.com/reprints. The authors declare no competing financial interests. Readers are welcome to comment on the online version of the paper. Correspondence and requests for materials should be addressed to F.Y. (francoyang1988@163.com).

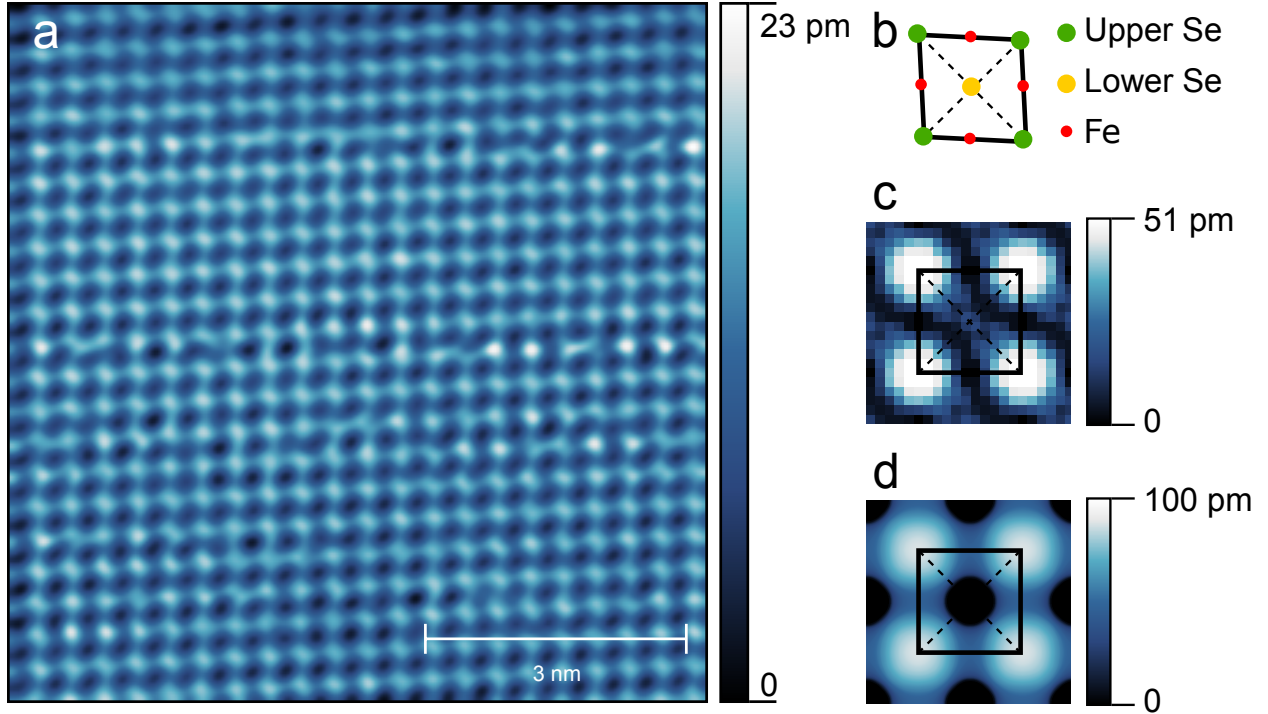


FIG. 1: **Structure of FeSe unit cell.** (a) STM-topography of impurity- and defect-free FeSe surface ($U=15$ mV $\gg \Delta$, $I=200$ pA). (b) Schematic drawing of the FeSe surface unit cell, which has C_2 rotational symmetry and two mirror planes (dashed lines). The nematic distortion of the unit cell is exaggerated in the figure. (c) STM-topography of FeSe of (2×2) surface unit cells extension obtained by averaging from original data of larger range ($U=5$ mV $> \Delta$, $I=2$ nA). (d) Simulated STM topography obtained from the LDOS calculated from first-principles.

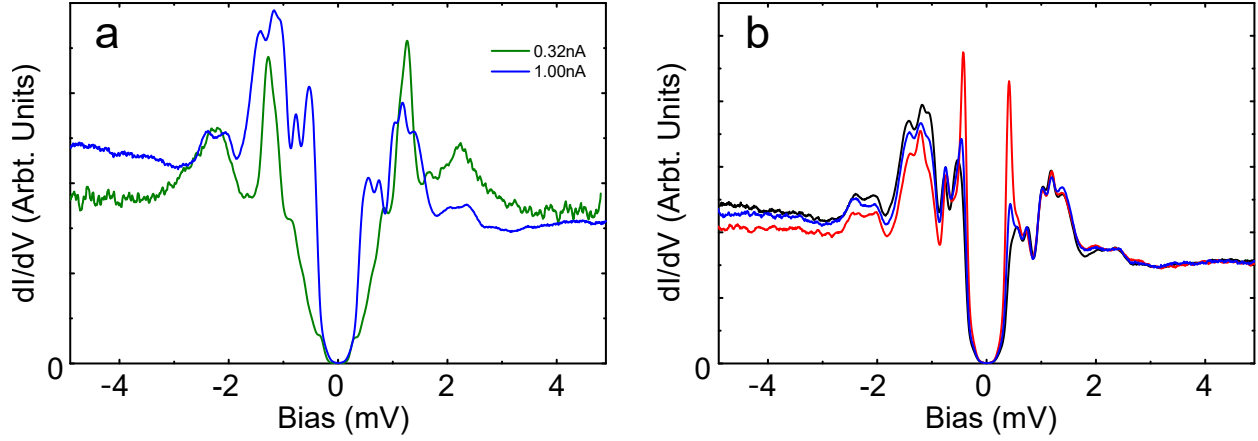


FIG. 2: **Differential conductance as function of tip-sample distance.** (a) Tunneling spectra recorded at 30 mK at different tip-sample distances. Feedback conditions for the green curve: $U=5 \text{ mV}$, $I=0.32 \text{ nA}$, blue curve: $U=5 \text{ mV}$, $I=1.00 \text{ nA}$. (b) Tunneling spectra at different lateral positions with feedback conditions $U=5 \text{ mV}$, $I=1 \text{ nA}$.

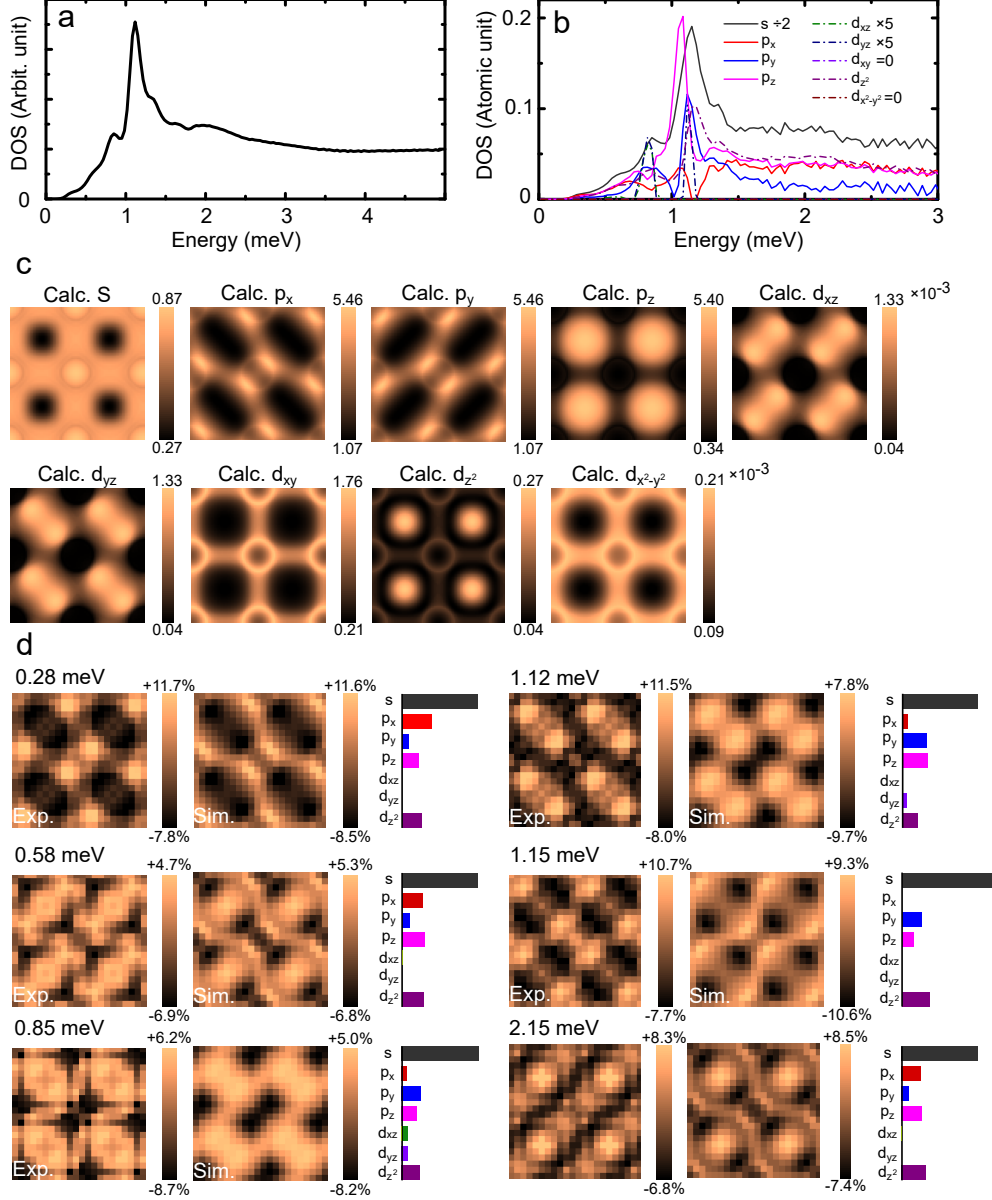


FIG. 3: **Orbitally resolved LDOS of the superconducting coherence peaks.**(a) Spatially averaged and symmetrized tunneling spectrum with feedback parameters $U=5$ mV, $I=2$ nA displaying several coherence peaks. (b) Fitted partial LDOS within the unit cell for s-, p- and d-states near the Fermi level revealing the orbital nature of the different peaks. (c) Partial LDOS of the different orbitals calculated on the iso-LDOS surface. This reflects the square of the Bloch wave function orbitally resolved. (d) Pairs of the experimental distribution of the LDOS in the unit cell in direct comparison with a fitted superposition of the calculated partial LDOS of c for energies as indicated. To the right of the pairs the fitting result of the relative contributions of the different orbitals is graphically displayed using the same colour code for the orbitals as in b. The experimental and theoretical distributions in the unit cell match nicely. From these fits, the partial LDOS of b was constructed.

Vanishing of orbital interference terms in the local density of states

In the following, we provide evidence for the assumption that no interference terms for tunneling electrons tunneling into orbitals exist. It implies that the local density of states is given by the sum of partial density of states of different orbitals α ,

$$\rho(\mathbf{r}, \omega) = \sum_{\alpha} \rho_{\alpha}(\mathbf{r}, \omega). \quad (1)$$

Our analysis assumes tetragonal crystal systems and is therefore applicable to bulk or surface electron systems hosted in FeSe as discussed in the main text. The result is furthermore based on the assumption that there is no (weak) spin orbit coupling. Finite spin orbit coupling may potentially alter the result such that interference terms are present. This aspect will be discussed in more detail at the end of this section.

The following analysis relies on group theoretical arguments and is therefore independent on the exact microscopic model. We start by expressing the local density of states probed in STM measurements in terms of the retarded single-particle correlator

$$\rho(\mathbf{r}, \omega) = -\frac{1}{V} \frac{1}{\pi} \sum_{\sigma} \text{Im} G_{\sigma\sigma}^R(\mathbf{r}, \mathbf{r}, \omega). \quad (2)$$

with spin index σ . Here, averaging over spin degrees of freedom assumes implicitly spin-rotational symmetry of the tip/probe system. Expressed in localized Wannier orbitals $\phi_{\alpha}(\mathbf{r})$ forming a complete set of single-particle states, the single-particle propagator reads

$$G_{\sigma\sigma'}^R(\mathbf{r}, \mathbf{r}', \omega) = \sum_{\alpha\beta} \sum_{ij} G_{\sigma\sigma', \alpha\beta}^R(\mathbf{R}_i, \mathbf{R}_j, \omega) \phi_{\alpha}(\mathbf{r} - \mathbf{R}_i) \phi_{\beta}^*(\mathbf{r}' - \mathbf{R}_j) \quad (3)$$

with orbital indices α, β and the location of Bravais lattice site \mathbf{R}_i (the extension to a n -dimensional basis is straightforward). In the following, we assume that the Wannier orbitals decay exponentially on length scales of the lattice spacing. It is therefore sufficient to consider the overlap of wave functions at the same lattice site $i = j$ only. In what follows, we will show that orbital off-diagonal terms, $\alpha \neq \beta$, of the single-particle correlator vanish,

$$G_{\sigma\sigma', \alpha \neq \beta}^R(\mathbf{R}_i, \mathbf{R}_i, \omega) = 0, \quad (4)$$

which leads to the vanishing of orbital interference terms in Eq. (1).

We consider the single-particle Hamilton operator represented in the Bloch basis by

$$H = \sum_{\mathbf{k}} \sum_{\alpha\beta} \epsilon_{\alpha\beta}(\mathbf{k}) d_{\alpha, \mathbf{k}}^{\dagger} d_{\beta, \mathbf{k}}, \quad (5)$$

with electronic creation-/annihilation operator $d_{\alpha,\mathbf{k}}^{(\dagger)}$ and orbital dependent dispersion relations $\epsilon_{\alpha\beta}(\mathbf{k})$. Electronic single-particle states are labeled by the crystal momentum \mathbf{k} and orbital indices α, β . We rewrite the Hamilton operator using operator bilinear forms $T^{(\Gamma)}(\mathbf{k}) = \sum_{\alpha\beta} d_{\alpha,\mathbf{k}}^\dagger \lambda_{\alpha\beta}^{(\Gamma)} d_{\beta,\mathbf{k}}$ with $(\lambda_{\alpha\beta}^{(\Gamma)})$ being matrices in orbital space, which transform under the point symmetry operations of the underlying lattice according to the one-dimensional irreducible representation $\Gamma \in \{A_1, A_2, B_1, B_2\}$,

$$H = \sum_{\mathbf{k}} \sum_{\Gamma} h^{(\Gamma)}(\mathbf{k}) T^{(\Gamma)}(\mathbf{k}). \quad (6)$$

Dispersion relations are contained in $h^{(\Gamma)}(\mathbf{k})$ which have well defined transformation behaviors depending on Γ . The single-particle correlator is consequently given by

$$G_{\alpha\beta}(z, \mathbf{k}) = [z - \sum_{\Gamma} h^{(\Gamma)}(\mathbf{k}) \lambda_{\alpha\beta}^{(\Gamma)}]^{-1}. \quad (7)$$

We now distinguish between contributions of trivial ($\Gamma = A_1$) and non-trivial ($\Gamma \neq A_1$) transformation behavior and rewrite the the previous equation by introducing the orbital matrix $\hat{G} = (G_{\alpha\beta})$ as

$$\hat{G}(z, \mathbf{k}) = \hat{G}_0(z, \mathbf{k}) + \hat{G}_0(z, \mathbf{k}) \hat{V}(\mathbf{k}) \hat{G}(z, \mathbf{k}) \quad (8)$$

$$= \hat{G}_0(z, \mathbf{k}) + \hat{G}_0(z, \mathbf{k}) \hat{V}(\mathbf{k}) \hat{G}_0(z, \mathbf{k}) + \dots \quad (9)$$

with $\hat{G}_0(z, \mathbf{k}) = [z - h^{(A_1)}(\mathbf{k}) \lambda^{(A_1)}]^{-1}$ and $\hat{V} = \sum_{\Gamma \neq A_1} h^{(\Gamma)}(\mathbf{k}) \lambda^{(\Gamma)}$.

We now consider the sum over crystal momenta of the correlator, $\sum_{\mathbf{k}} G_{\alpha\beta}(\mathbf{k}, z) = G_{\alpha\beta}(\mathbf{R}_i, \mathbf{R}_i, z)$, which is identical to its previously introduced real space version. By inspecting Eq. (9), we find that $\sum_{\mathbf{k}} G_{\alpha\beta}(z, \mathbf{k}) = 0$ for $\alpha \neq \beta$, where each term vanishes individually. This finding is traced back to the fact that either (I) the resulting matrix in orbital space is diagonal, or (II) the sum over crystal momenta of a non-trivially transforming function vanishes, $\sum_{\mathbf{k}} G^{(\Gamma)}(\mathbf{k})|_{\Gamma \neq A_1} = 0$. In particular, the first term vanishes because of (I); the second because of (II), $\sum_{\mathbf{k}} [h^{(A_1)}(\mathbf{k})]^2 h^{(\Gamma \neq A_1)}(\mathbf{k}) = 0$; the third because of (I) for $\Gamma = \Gamma'$ and because of (II) for $\Gamma \neq \Gamma'$, $\sum_{\gamma\mathbf{k}} h^{(\Gamma)}(\mathbf{k}) h^{(\Gamma')}(\mathbf{k}) \lambda_{\alpha\gamma}^{(\Gamma)} \lambda_{\gamma\beta}^{(\Gamma')}|_{\Gamma \neq \Gamma'} = 0$. The identical reasoning can be applied to any higher order term by noticing that if the orbital matrix is non-diagonal the product of h 's contains an odd number of non-trivially transforming functions. This eventually implies Eq. (4).

In the case of finite spin orbit coupling, when the spin degrees of freedom cease to be good quantum numbers, the result is potentially altered. In the presence of inversion symmetry,

which holds true for electronic bulk states in the tetragonal crystal system, all bands are still doubly degenerate and the Hamilton operator can be rewritten in terms of bilinear form transforming according to one-dimensional representations. However, this potentially changes when the inversion symmetry is broken, which is especially the case when electronic surface states being probed in STM measurements. Here, the surface state band's degeneracy may be lifted. Furthermore, the orbital character of electronic states of the STM tip has to be taken into account. The average over spin states in Eq. (2) is replaced by a weighted average depending on the STM tip's orbital character and a cancellation of contributions is not guaranteed. For this more complex scenario, the previously drawn conclusion manifesting in Eq. (1) loses its rigidity and orbital interference terms may appear as function of the strength of spin-orbit interaction.